

Design approach for a FRP structural formwork based steel-free modular bridge system

Lijuan Cheng[†]

Department of Civil and Environmental Engineering, University of California, Davis, CA 95616, USA

Vistasp M. Karbhari[‡]

Department of Structural Engineering, University of California, San Diego, La Jolla, CA 92093-0085, USA

(Received August 8, 2005, Accepted June 29, 2006)

Abstract. The paper presents results of parametric studies, and an overall approach for the design of a modular bridge system which incorporates a steel-reinforcement free concrete slab cast on top of carbon FRP stiffened deck panels which act as both structural formwork and flexural reinforcement, spanning between hollow box type FRP girders. Results of the parametric studies are highlighted to elucidate important relationships between critical configurational parameters and empirical equations based on numerical studies are presented. Results are discussed at the level of the individual deck and girder components, and as a slab-on-girder bridge system. An overall design methodology for the components and bridge system including critical performance checks is also presented.

Keywords: steel-free; fiber reinforced polymer; structural formwork; parametric study; design approach; modular bridge system.

1. Introduction

The critical need for rehabilitation, and even replacement, of a large portion of the nation's bridge inventory has led to a focused effort towards the development and implementation of bridge systems incorporating newer and potentially more durable materials. Fiber reinforced polymer (FRP) composites are increasingly being considered in this effort. Decks fabricated of FRP composites have been extensively characterized and systems incorporating these decks have been implemented in the field. However, to date, the FRP decks are significantly more expensive than conventional reinforced concrete decks (GangaRao *et al.* 1999, Karbhari *et al.* 2000). In an attempt to combine the attractive features of FRP composites with the low-cost and good compressive characteristics of concrete, a steel-free modular bridge system has been developed wherein a steel-reinforcement free concrete slab is cast on top of carbon FRP stiffened deck panels which act as both structural framework and as the flexural reinforcement (Cheng *et al.* 2005). The deck panels span between girders, and a system incorporating FRP hollow box type girders has been extensively characterized

[†] Assistant Professor, E-mail: dawcheng@ucdavis.edu

[‡] Professor, Corresponding author, E-mail: vkabhari@ucsd.edu

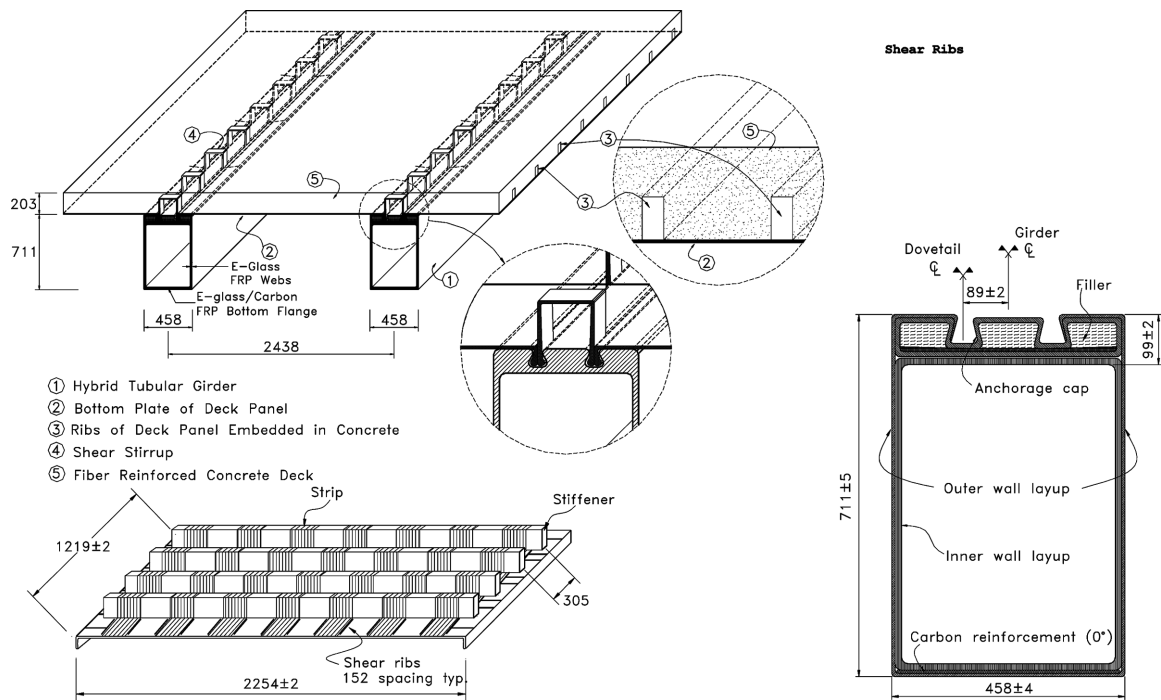


Fig. 1 Components of the bridge system

through large scale component and system tests (Cheng *et al.* 2005, Cheng and Karbhari 2005), which show the structural validity and effectiveness of the modular system (Fig. 1). It is noted that Dieter *et al.* (2002) and Kwon *et al.* (2004) reported on the use of FRP stay-in-place forms for bridge decks but both these were additionally reinforced with FRP grids and bars taking the place of steel reinforcing bars.

The system has been characterized, and the performance validated, through tests of individual deck panels, girders, and a two-girder-deck assemblage system (Cheng *et al.* 2005) as well as fatigue tests conducted to assess system response. To understand performance under traffic loads that induce repetitive stress cycles, a two span deck specimen (of 1.22 m width) was also tested by subjecting it to a total of 2.36 million cycles of load simulating an AASHTO design truck (AASHTO 2004) and the system was shown to have extremely stable response, far exceeding the demand levels (Cheng and Karbhari 2005). For further implementation and future adoption of such classes of systems, suitable analysis and design tools, amenable for use in routine bridge design are essential. This paper presents a simplified design approach and a description of an appropriate set of analytical tools for use with the modular system. Results from a parametric study conducted on both individual components and the slab-on-girder system are presented, and then the simplified design methodology for the system is elucidated.

2. Parametric studies

In an attempt to enhance an understanding of response, and as an aid to selection of appropriate

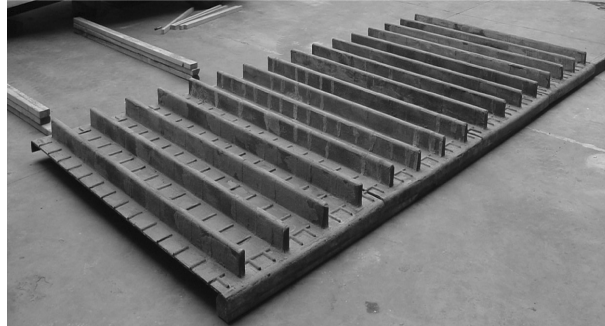


Fig. 2 FRP Stiffened deck panel

parameters, parametric studies were carried out at the level of the deck, girder, and the system. Details of the analysis and comparisons with experiments to show validity are reported elsewhere (Cheng *et al.* 2005, Cheng and Karbhari 2005) and are hence not repeated herein except to elucidate specific points.

2.1 Reinforcement free concrete deck on FRP structural formwork

The functionality of the deck systems arises from the intrinsic continuity and stress transfer between the FRP structural formwork (Fig. 2) and the concrete cast on top, which is ensured through shear. This is maintained through both a sand roughened surface on the panel, and through raised ribs. An analytical model of the deck takes advantage of symmetry, and uses ABAQUS (2003), with the deck panel modeled using 4-node double curved general-purpose shell elements with reduced integration points (S4R) and the concrete by 8-node linear brick elements (C3D8). Linear elastic orthotropic properties are used for the FRP composite, while a “damaged” plasticity formulation is used to model the nonlinear response of concrete. This uses the ABAQUS (2003) formulation incorporating isotropic damaged elastic response in combination with isotropic tensile and compressive plasticity to represent inelastic behavior of concrete.

The rough, sand based, surface on the FRP panel induces a frictional effect which is simulated using the classic Coulomb model in combination with the definition of surface interaction used in ABAQUS (2003). The two contacting surfaces, the FRP deck and the concrete, are assumed to carry shear stresses up-to a level of critical shear stress, τ_{crit} , at which point sliding initiates as a function of the contact pressure, p , between the surfaces, such that

$$\tau_{crit} = \mu p \quad (1)$$

where μ is the coefficient of friction, which was experimentally determined to be 0.562.

The interlock provided by the raised shear ribs is simulated through use of spring elements acting between the nodes of elements on the panel and slab, with the line of action being the line joining the two nodes. Thus, the relative displacement along this line represents the relative slippage between the two surfaces. The behavioral property of these spring elements is represented by a bond strength-slippage relationship wherein the springs are assumed to behave in a linear elastic fashion prior to attainment of their ultimate capacity. After that, sudden failure occurs with a large drop in load and the spring stiffness (i.e., force per relative displacement) reduces to zero. The spring

stiffness during the elastic range, k_s , is defined by the shear bond strength of the interface, τ_{is} , which was assumed to be 50 MPa/mm based on extensive experimental data for CFRP-concrete interfaces (Yoshizawa *et al.* 2000). The ribs fabricated from sand-filled epoxy, as shown in Fig. 2 and described in Cheng *et al.* (2005) and Cheng and Karbhari (2005) are externally formed on the composite deck panel through the use of epoxy resin and therefore the ultimate shear strength or capacity of the rib-panel interface, τ_{is} , can be assumed to be governed by the nominal shear strength of the epoxy resin. The ribs are a minimum of 7 mm in height and 15 mm in width and are generally spaced 152 mm on centers to enhance shear interlock with concrete. The ribs are formed of the same resin as used for the fabrication of the deck panel and in the ideal case are formed at the same time thereby providing a primary, rather than secondary, bond. Comparative experiments conducted on specimens with ribs at different spacings indicate that the response is similar within the spacing range of 150-305 mm.

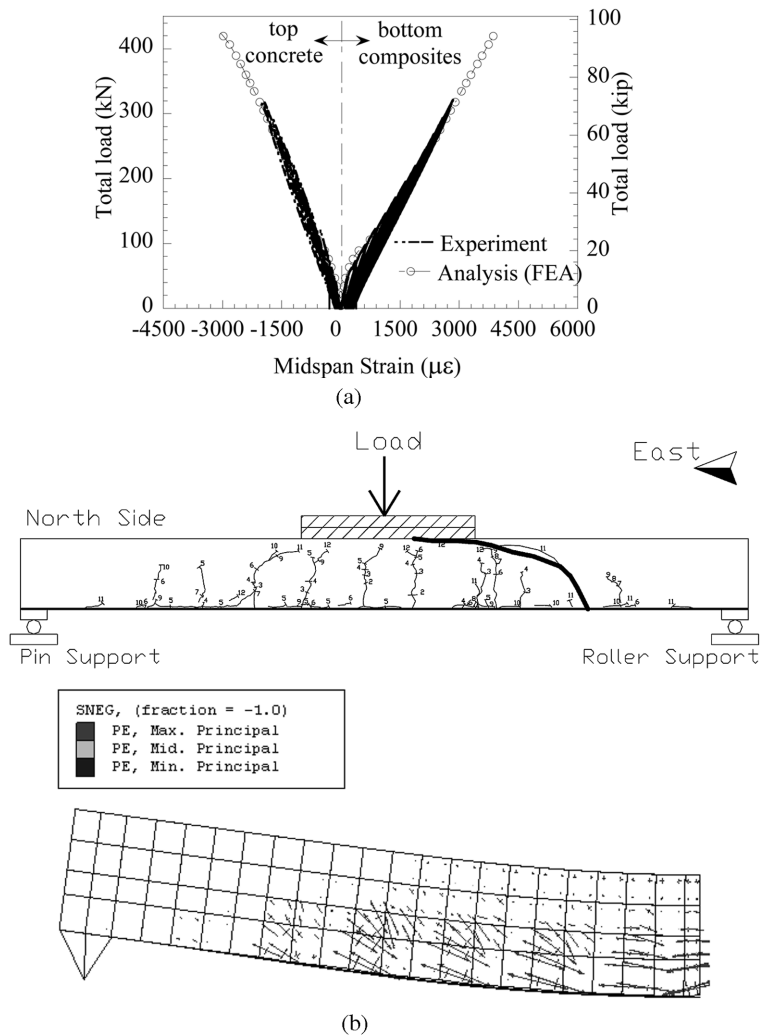


Fig. 3 Response of the steel-free FRP-concrete deck panel; (a) Comparison of FEA results with experiments, (b) Comparison of crack patterns

Table 1 Parameters used in deck panel study

Parameter	Range/Level	Rationale
f'_c	16.5 MPa - 68.9 MPa	Upper and lower bounds correspond to the AASHTO defined allowable range
a/d ratio	2.5 - 6.5	a/d controls failure and the range corresponds to that typical for inclined flexural-shear type failure (MacGregor 1997)
Carbon reinforcement	4-12 layers (resulting in a plate thickness of 4.37-7.42 mm)	Variable ranges from manufacturing, structural stiffness, and cost

Results from the model are seen to compare well with experiments in flexure under a central line load (Cheng 2005) and examples of strain and crack patterns are seen in Figs. 3(a) and 3(b) respectively. It should be noted that in Fig. 3(b) the graphical representation of predicted cracking is shown by vectors normal to the crack plane, and the overall trend that can be predicted for crack location and level can be seen to match well with the experimentally measured crack patterns shown in the same figure.

While a number of materials and configuration related parameters can be selected for study, from an applications/field perspective the most important are the tensile strength of the concrete (since this will control cracking at the FRP panel-concrete interface), the shear span-to-depth ratio (a/d), and the level of carbon fiber reinforcement used (ρ_c , since this intrinsically controls stiffness). Effects of shear-rib spacing were reported by Cheng (2005) and hence a detailed study is not considered herein. These are then used for the parametric study, with ranges shown in Table 1. It is noted that since a direct relation exists between concrete compressive strength, f'_c , and tensile strength, the compressive strength, which is easily characterizable, is used as a primary parameter.

The effect of change in concrete strength on overall response of the component is shown in Fig. 4, for strength levels corresponding to the extremes of the range recommended by AASHTO (2004) as well as an intermediate value corresponding to the level used in earlier experiments (Cheng 2005). Over the entire range it can be noted that the effect of an increase in concrete

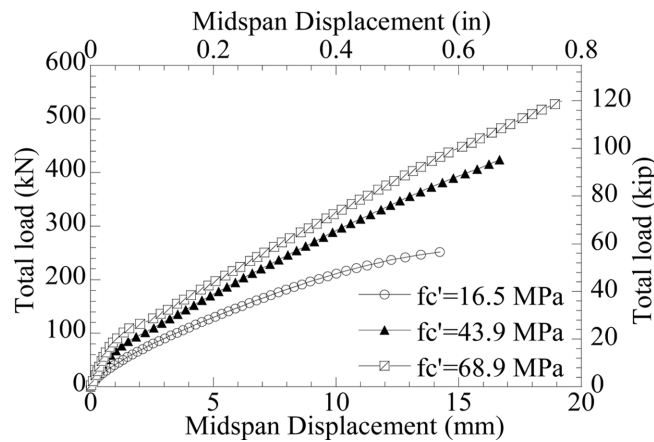


Fig. 4 Effect of concrete strength on deck response at a rib spacing, s , of 152 mm

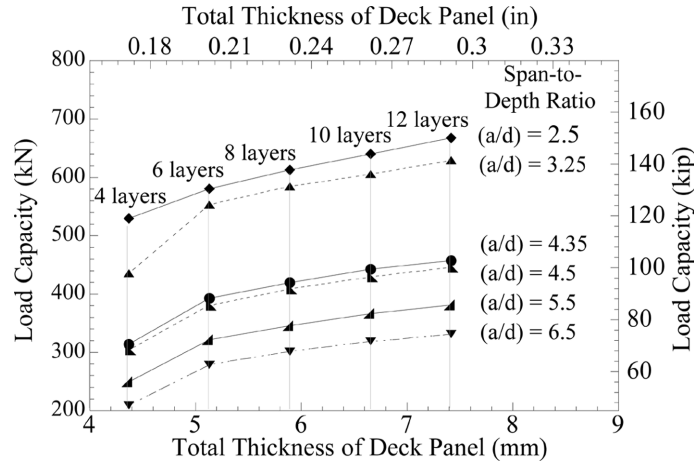


Fig. 5 Effect of amount of carbon fiber reinforcement on deck response at a rib spacing, s , of 152 mm

strength is greater for lower values of f'_c and decreases as f'_c increases following a simple exponential relationship

$$P_{deck} = 57.65 \cdot (f'_c)^{0.526} \quad (2)$$

where P_{deck} denotes the failure load for the steel free FRP-concrete deck panel. It is noted that final failure in all cases was due to concrete crushing.

As can be expected, an increase in the thickness of the FRP panel's plate component results in a corresponding increase in the total amount of carbon fiber used, although the fiber fraction remains constant, which causes an increase in stiffness. Fig. 5 shows the effect of this change over the range of span-to-depth ratios considered. As can be seen the increase in load capacity is fairly linear with thickness except for the initial region of 4-6 layers wherein the panel shows a much greater rate of increase. The trends and slopes within the 6-12 layer thickness regime are actually similar for rib spacing between 152 mm and 305 mm, after which the lack of sufficient interlock, which is provided by the raised shear ribs causes premature loss in continuity between the two components – the FRP deck and the concrete, resulting in failure by mechanisms other than the concrete crushing. Within the 152 mm to 305 mm range, however the increase in spacing decreases load capacity by only 3-7%.

2.2 FRP girder

Although the FRP-concrete deck system could be used in conjunction with girders fabricated of a number of materials, in this study hollow rectangular tube type girders with a configuration as shown in Fig. 1 are considered. The primary reinforcement used was E-Glass fiber in the triaxial (0/–45/45) and unidirectional fabric form with additional unidirectional carbon fabric embedded in the bottom flange for added stiffness. The effective mechanical properties of the girder components are listed in Table 2. Element 1 consists of the bottom flange, element 2 is representative of a web of the box section, element 3 comprises all the layers in the bottom portion of the cap region, element 4 is representative of an outer side of the cap, element 5 consists of the layers in the top

Table 2 Effective properties of girder component

Property	Element 1	Element 2	Element 3	Element 4	Element 5
Longitudinal modulus, E_L	42069 MPa	14000 MPa	15862 MPa	14621 MPa	14621 MPa
Transverse modulus, E_T	12276 MPa	12552 MPa	12138 MPa	12552 MPa	12552 MPa
In-plane shear modulus, G_{LH}	4448 MPa	4428 MPa	3538 MPa	4145 MPa	4145 MPa
In-plane Poisson's ratio, ν_{LH}	0.31	0.33	0.30	0.31	0.31
In-plane Poisson's ratio, ν_{HL}	0.13	0.30	0.23	0.27	0.27
Nominal thickness, t	25 mm	19 mm	32 mm	16 mm	16 mm

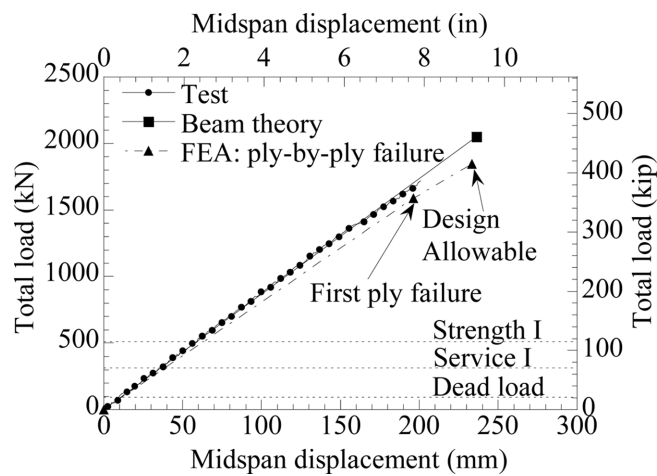


Fig. 6 Load-midspan displacement response of a single girder

portion of the cap region. Details of the large-scale tests conducted on the girder for purposes of characterization are reported in Cheng *et al.* (2005).

A half-span FEA model using symmetry was created using four-node shell elements, S4R, for the composite and 8-node solid elements, C3D8, for the polymer concrete filled regions in the girder cap. The FRP composite response was modeled by defining lamina properties for each layer and the computing structural response through a three-stepped method: (1) micromechanical analysis of individual layers following classical lamination theory, (2) structural response assessment using FEA with these properties using the Tsai-Wu criterion, and (3) post-processing of response to identify the failure load. As seen in Fig. 6, the analytical results match the experimental response in flexure fairly well, with failure being predicted when strain in the carbon fiber reinforcement reaches the design ultimate of 1% at a load of 1844 kN which compares well within 8% of the experimentally determined failure load. The first-ply failure load, which corresponded to the initiation of failure, was noted at a load of 1588 kN.

Within the confines of realistic changes in configuration, the parametric study considered changes in the thickness of carbon fiber reinforcement (between 0 layers and 27 layers), overall depth of the girder (from 356 mm to 1422 mm, maintaining a fixed cap depth of 99 mm), and span length (from 6 m to 38 m, corresponding to the limits for short span bridges). It should be noted that the experimentally characterized girder had an overall depth of 711 mm with a cap depth of 99 mm, a

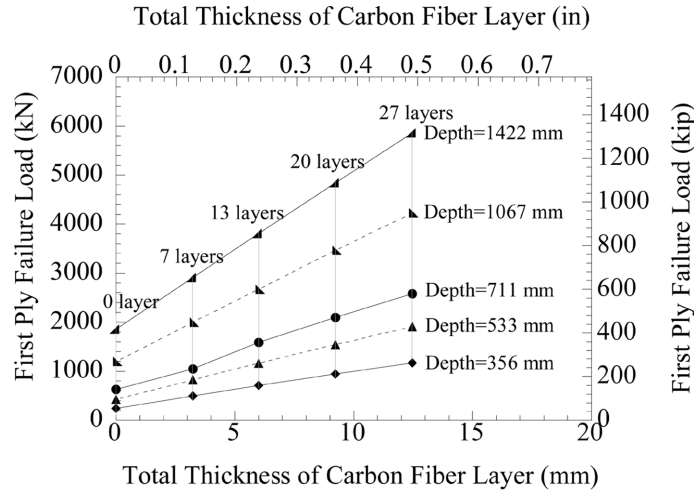


Fig. 7 FPF load as a function of carbon fiber reinforcement and girder depth

width of 458 mm, 13 layers of carbon fabric reinforcement (at a total thickness of 5.85 mm), and a span of 8.5 m (Cheng *et al.* 2005).

Considering the simplest case of just increasing the number of layers of carbon fiber reinforcement on the tension side, keeping all other variables constant, as expected, the first ply failure (FPF) load can be shown to increase almost linearly with increase in thickness (i.e., increase in the number of layers of carbon fabric, keeping fiber volume fraction constant). In all cases the ply showing failure is the bottom-most in the girder itself, indicating that although the increase in carbon reinforcement results in an increase in both strength and stiffness, it does not change the mode and mechanism of FPF. It is of obvious interest to compare and contrast the effect of change in the girder depth (essentially through increase in web height which incorporates only the cheaper E-glass fiber reinforcements) with the change in number of layers of carbon fabric. This is shown for the experimentally verified span of 8.5 m in Fig. 7. As can be seen there is a greater effect of increasing the number of carbon fiber layers for girders with greater depth than for shallower ones, and in fact this is also seen in the rate of increase in FPF load with increase in the number of carbon fiber layers at the largest depth (1422 mm). From a preliminary design perspective it is of interest to note that, for the general configuration considered, the FPF load can be empirically determined using a simple relationship

$$\text{FPF Load} = [0.039545 \cdot d^{1.4796}] + \left(\frac{d}{4.5}\right)t \quad (3)$$

where d is the girder depth and t the thickness of the carbon reinforcement layer (both in mm). The R^2 correlation between the computational predictions and the empirical equation are seen to exceed 0.999 in all cases, indicating very good correspondence. The use of this equation thus provides a simple means of enabling the designers to make quick decisions between depth and carbon reinforcing layers for purposes of preliminary design.

The use of prefabricated modules for construction of bridges is extremely attractive, especially if the modules can be rapidly assembled and even transported easily to site. The current system provides this since the use of FRP decreases weight substantially, the modules are easily snapped

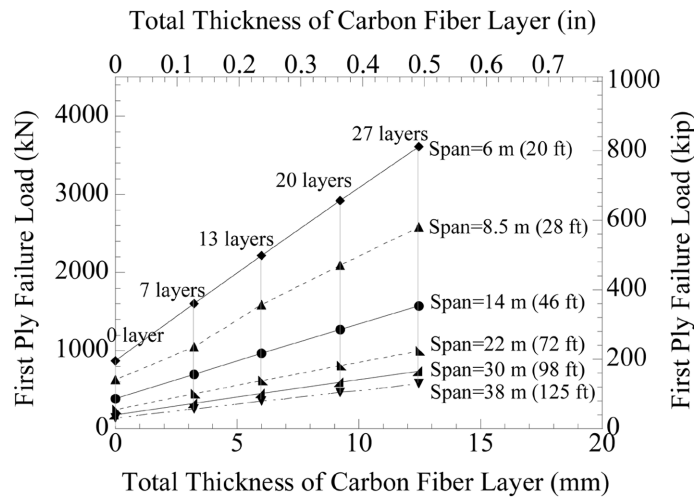


Fig. 8 FPF load as a function of carbon fiber reinforcement and span length

together, and the concrete deck can be rapidly cast since no reinforcement cages (as with steel) have to be assembled. The current configuration lends itself well to short span bridges wherein the typical range for the slab-on-girder class is 6-38 m (Taly 1998). With an increase in span the FRP load will decrease, and it is of interest to assess effects of parameters of number of layers of carbon fabric and span length as in Fig. 8, for a girder depth of 711 mm, from which it can be seen that the increase in FPF load with increase in carbon fabric layers is much more significant at shorter spans while depth increases are necessary at the longer spans. From a preliminary design perspective the overall relationship between the parameters can be empirically expressed as

$$FPF \text{ Load} = \left[\frac{(0.336d^{1.4796}) + (1.88dt)}{Span} \right] \tag{4}$$

where d and t are in mm and the span is in meters. It is noted that Eqs. (3) and (4) provide empirical estimates for relationships between parameters for the purpose of initial design and must hence be considered as approximations. A complete set of empirical equations and charts resulting from in-depth parametric studies will be reported elsewhere.

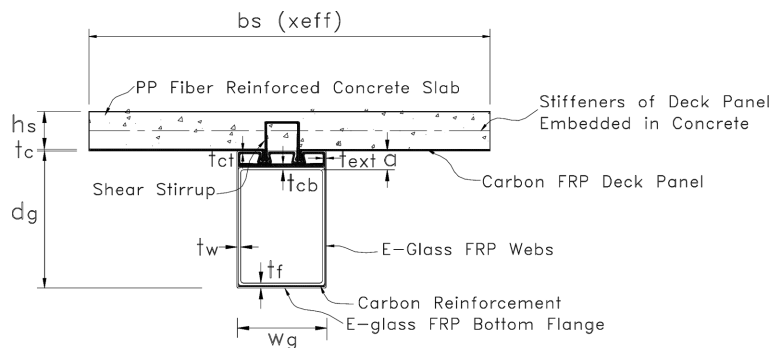


Fig. 9 Schematic of typical slab-on-girder

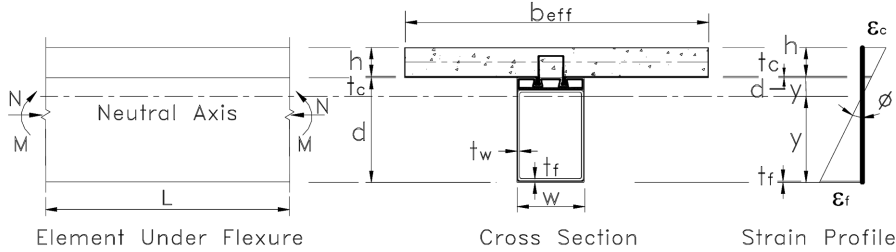


Fig. 10 Strain distribution

2.3 Slab-on-girder system

Fig. 9 depicts a typical section of a slab-on-girder configuration for the current system. In this d_g is the total girder depth, h_s is the depth of the concrete slab not including the thickness of the CFRP panel, t_c , b_s is the flange width with efficiency of the compressive flange, e_{ff} , w_g is the girder width, a is the depth of the anchorage zone, s is the distance between the center-lines of the grooves in the cap region, t_f is the thickness of the girder bottom flange, t_w is the thickness of the girder web, t_{cb} is the thickness of the cap bottom flange, t_{ct} is the thickness of the cap top flange, and t_{ext} is the thickness of the caps exterior web. For purposes of analysis the equivalent moduli are used for the FRP components corresponding to the operative direction. A schematic of the section with strain profile used in sectional analysis is shown in Fig. 10. The sectional analysis essentially involves an iterative procedure of adjusting the neutral axis position for a given strain distribution to maintain force equilibrium.

Since shear-lag affects the FRP-concrete deck component its strength is not fully realized by the system and hence an effective slab width is typically used for analysis as

$$b_{eff} = e_{ff} b_s \tag{5}$$

where e_{ff} is the slab efficiency coefficient. Results of different coefficients for the 711 mm depth

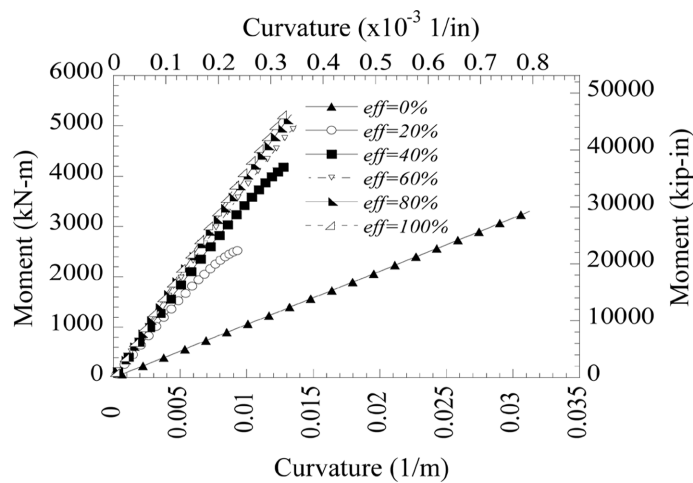


Fig. 11 Effect of slab width efficiency on $M-\phi$ response

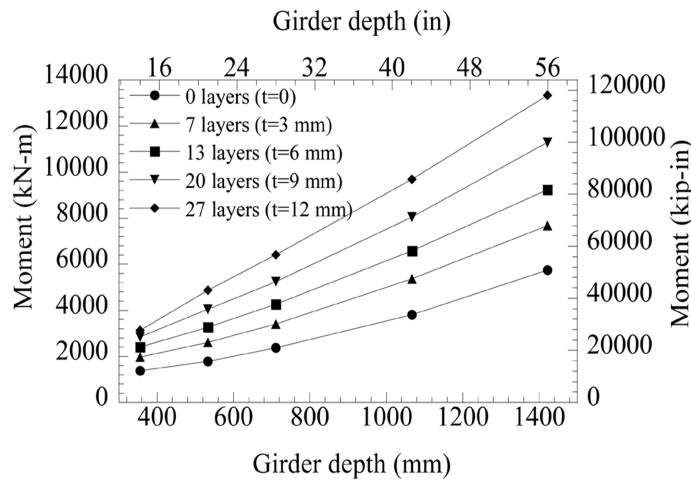


Fig. 12 Moment capacity as a function of girder depth and carbon fiber reinforcement

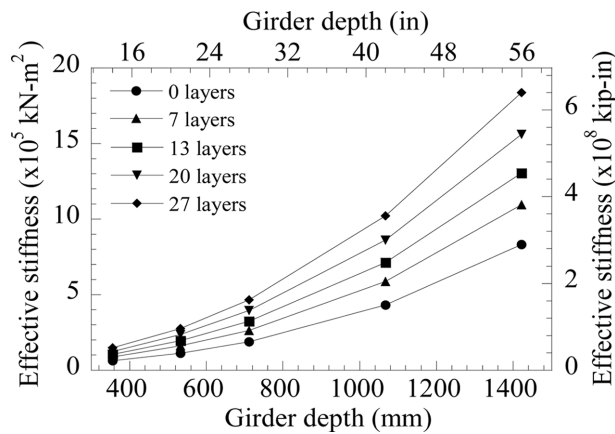


Fig. 13 Effective stiffness (M/ϕ) as a function of girder depth and carbon fiber reinforcement

girder (discussed in the previous sections) with a 6 mm carbon fiber reinforcement thickness are given as a typical example in Fig. 11 from which it can be seen, as expected, that although moment capacity increases with slab width efficiency, the increase is less after about 50% efficiency. Assuming an effective slab width of 80% the effect of thickness of the carbon fiber reinforcement and girder depth on moment capacity and effective stiffness are shown in Figs. 12 and 13, respectively. These charts, in conjunction with ones discussed earlier, provide a means for further development of design and analysis tools for the use of such systems.

3. Simplified design approach for the deck

While parametric studies provide useful charts for extrapolation of the “as-tested” design, a more comprehensive approach is needed for actual routine design of the system by engineers. An approach is elucidated in this section.

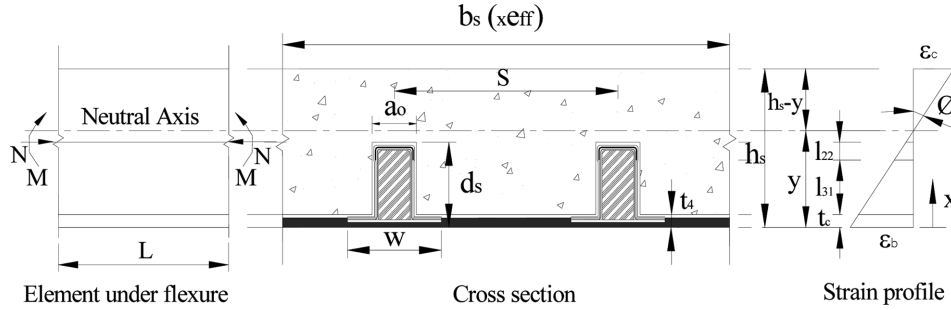


Fig. 14 Schematic of typical FRP-concrete deck section and strain profile

The FRP deck panel provides the primary component that carries construction loads (weight of wet concrete, equipment, live load etc.) prior to the setting of the concrete. Maximum stress, and strain, levels in the deck under bending and shear can be computed using elastic analysis and sectional analysis (for example, as in McCormac and Nelson 1999). Once the concrete sets, the hybrid reinforcement-free concrete slab and the stiffened FRP panel act as a unit and can be designed for the requisite flexural capacity while ensuring that the FRP panel does not fail in a brittle mode. This can be ensured through achievement of compressive strain in concrete, ϵ_c , reaching 0.003, prior to the ultimate strain, ϵ_s , being reached in the composite, thus causing a compression failure. Flexural capacity, M_u , can be obtained as a simple summation of internal moments of forces along the cross-section (Fig. 14 shows a typical section). The AASHTO (2004) specified rectangular stress block is used with a mean stress of $0.85 f'_c$ and a depth of a_1 , where

$$\frac{a_1}{c} = \beta_1 = 0.85 \quad \text{for } f'_c \leq 27.6 \text{ N/mm}^2 \quad (6)$$

where β_1 is reduced continuously by 0.05 for each increment of 6.89 N/mm^2 in strength in excess of 27.6 N/mm^2 (ACI 1995) to account for the less favorable stress-strain response in higher strength concrete. Flexural capacity of the cross-section can then be based on evaluation of cross-sectional equilibrium at the limit state ($\epsilon_c = \epsilon_c^u$) using this equivalent stress block approach. Tensile strength of the concrete is neglected at this stage, being substantially less than that of the FRP components. For simplification, and generality, the average of the FRP moduli and thickness of the upper and lower parts of the FRP stiffener are used. Normal strain and stress distributions corresponding to three cases for ultimate flexural capacity, corresponding to when the neutral axis is located above the rectangular stiffeners, within the stiffeners, or within the bottom plate, are illustrated in Fig. 15. Flexural capacity is then calculated from equilibrium principles and a summary for the three cases is given in Eqs. (7)-(14) for the three cases.

When the neutral axis is located above the rectangular stiffeners (Fig. 15(a))

$$\begin{aligned} \epsilon_c &= \epsilon_c^u, \quad \epsilon_4 < \epsilon_4^u \\ \epsilon_4 &= \frac{y_u}{h - y_u} \epsilon_c^u \end{aligned} \quad (7)$$

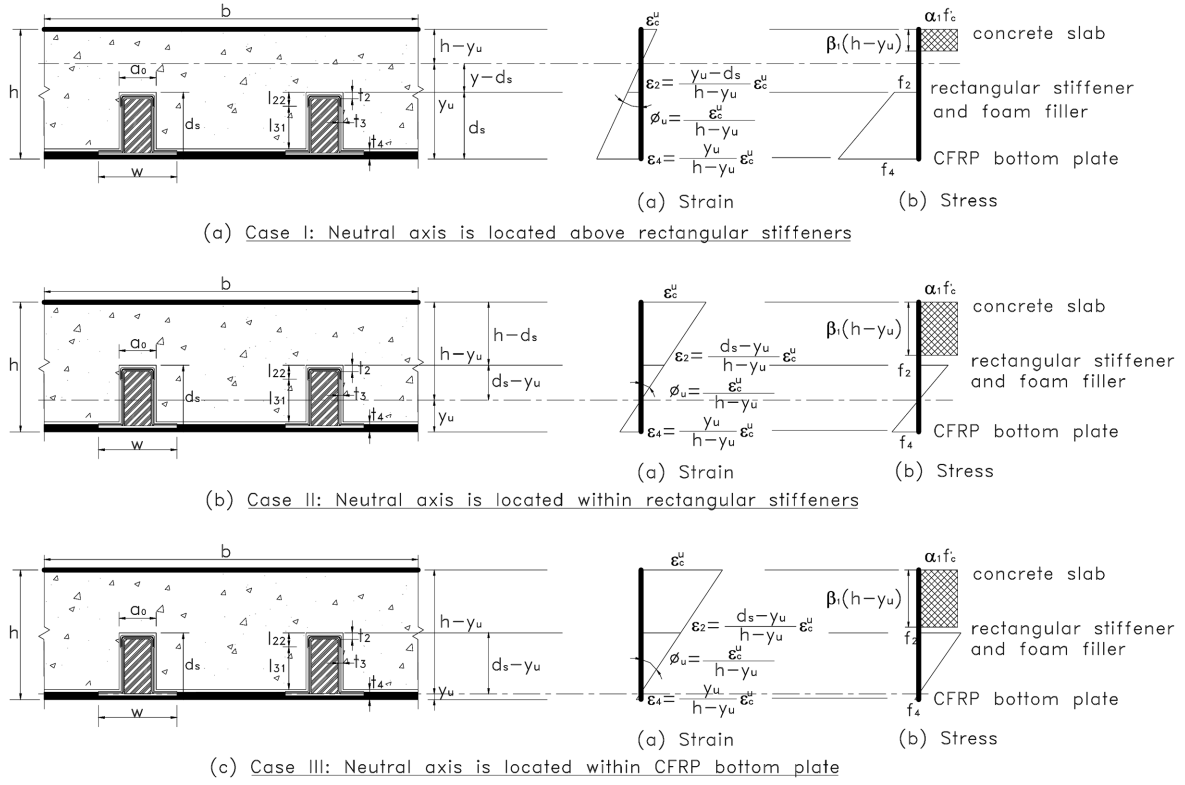


Fig. 15 Stress and strain distribution at ultimate for the FRP-concrete deck

$$\varepsilon_2 = \frac{y_u - d_s}{h - y_u} \varepsilon_c^u$$

$$y_u = h + C_2 / (2C_1) - [4C_1(hC_2 - C_3) + C_2^2]^{1/2} / (2C_1) \quad (8)$$

$$M_u = 0.85f_c' \beta_1 b (h - y_u) [h - \beta_1(h - y_u)/2] - \varepsilon_c^u / (h - y_u) \{ 2E_s t_s [a_o d_s (y_u - d_s) + d_s^2 (y_u - d_s/2) + (w - a_o)(t_4 + t_s/2)y_u] + E_4 b t_4^2 y_u / 2 + E_f a_o d_s^2 (y_u - d_s/2) \}$$

where

$$C_1 = 0.85f_c' \beta_1 b / \varepsilon_c^u \quad (9a)$$

$$C_2 = 2E_s t_s (2d_s + w) + E_4 t_4 b + 2E_f a_o d_s \quad (9b)$$

$$C_3 = 2E_s t_s (a_o + d_s) d_s + E_f a_o d_s^2 \quad (9c)$$

When the neutral axis is located within the rectangular stiffener (Fig. 15(b)),

$$\varepsilon_2 = \frac{d_s - y_u}{h - y_u} \varepsilon_c^u \quad (10)$$

$$y_u = [C_2 - (C_2^2 - 4C_3C_4)^{1/2}] / (2C_4)$$

$$M_u = 0.85f_c' \beta_1 \left\{ b(h - d_s) \left[h - \frac{\beta_1(h - d_s)}{2} \right] + (d_s - y_u)(b - 2a_o) \left[d_s - \frac{\beta_1(d_s - y_u)}{2} \right] \right\} \\ + \frac{\varepsilon_c^u}{h - y_u} \left\{ 2E_s t_s \left[ad_s(d_s - y_u) + \frac{(d_s - y_u)^2(d_s + y_u)}{2} - \frac{y_u^3}{2} - y_u(w - a_o) \left(t_4 + \frac{t_s}{2} \right) \right] \right\} \\ \left. + E_f a_o [(d_s - y_u)^2(d_s + y_u) - y_u^3] / 2 - E_4 t_4^2 b y_u / 2 \right\} \quad (11)$$

where

$$C_1 = 0.85f_c' \beta_1 / \varepsilon_c^u \quad (12a)$$

$$C_2 = 2C_1(bh - a_o h - ad_s) - 2E_s t_s(2d_s + w) - E_4 t_4 b - 2E_f a_o d_s \quad (12b)$$

$$C_3 = C_1(bh - 2a_o d_s)h + 2E_s t_s(a_o + d_s)d_s + E_f a_o d_s^2 \quad (12c)$$

$$C_4 = C_1(b - 2a_o) \quad (12d)$$

When the neutral axis is located within the CFRP bottom plate (Fig. 15(c)),

$$y_u = [(C_2^2 + 4C_3C_4)^{1/2} - C_2] / (2C_4) \quad (13)$$

$$M_u = 0.85f_c' \beta_1 \left\{ b(h - d_s) \left[h - \frac{\beta_1(h - d_s)}{2} \right] + (d_s - t_4)(b - 2a_o) \left[d_s - \frac{\beta_1(d_s - t_4)}{2} \right] \right\} \\ + \frac{\varepsilon_c^u}{h - y_u} \left\{ 2E_s t_s \left[ad_s(d_s - y_u) + \frac{d_s(d_s - y_u)(d_s + t_4)}{2} + y_u(w - a_o) \left(t_4 + \frac{t_s}{2} \right) \right] \right\} \\ \left. + E_f a_o d_s(d_s - y_u)(d_s + t_4) / 2 + E_4 b y_u(t_4^2 / 2 + y_u^2) \right\}$$

where

$$C_1 = 0.85f_c' \beta_1 [bh - 2a_o d_s - t_4(b - 2a_o)] / \varepsilon_c^u \quad (14a)$$

$$C_2 = 2E_s t_s(d_s + 2w - a_o) + E_f a_o d_s - E_4 t_4 b + C_1 \quad (14b)$$

$$C_3 = 2E_s t_s(a_o + d_s)d_s + E_f a_o d_s^2 + C_1 h \quad (14c)$$

$$C_4 = 2E_4 b \quad (14d)$$

Table 3 Comparison of design equations

Formulae	Design equations	R-square value
ACI code	$\frac{V_u s}{bd'} = \frac{19.983 \rho_c d'}{L'} + 0.0139 \sqrt{f'_c}$ ($s = 152$ mm)	0.63
$\frac{V_u s}{bd'} = \frac{m \rho_c d'}{L'} + k \sqrt{f'_c}$	$\frac{V_u s}{bd'} = \frac{44.509 \rho_c d'}{L'} + 0.0206 \sqrt{f'_c}$ ($s = 305$ mm)	0.88
Schuster's formula	$\frac{V_u s}{bd'} = \frac{0.109 d'}{L'} \sqrt{f'_c} + 2.188 \rho_c$ ($s = 152$ mm)	0.89
$\frac{V_u s}{bd'} = \frac{m d'}{L'} \sqrt{f'_c} + k \rho_c$	$\frac{V_u s}{bd'} = \frac{0.211 d'}{L'} \sqrt{f'_c} + 4.190 \rho_c$ ($s = 305$ mm)	0.89
Zsutty's formula	$\frac{V_u s}{bd'} = 0.750 \left(\frac{f'_c \rho_c d'}{L'} \right)^{1/3} - 0.366$ ($s = 152$ mm)	0.92
$\frac{V_u s}{bd'} = m \left(\frac{f'_c \rho_c d'}{L'} \right)^{1/3} + k$	$\frac{V_u s}{bd'} = 1.511 \left(\frac{f'_c \rho_c d'}{L'} \right)^{1/3} - 0.770$ ($s = 305$ mm)	0.91

Table 4 Comparison between predictions using design equations and experiments

Rib spacing	ACI code	Schuster's formula	Zsutty's formula	Experimental average
$s = 152$ mm	347.6 kN	343.1 kN	205.9 kN	321.4 kN
$s = 305$ mm	334.0 kN	330.1 kN	181.1 kN	327.8 kN

Since the integrity of the deck system depends on shear-bond between the FRP panel and the concrete, the level of shear bond needs to be checked. This can be done using results from parametric studies (as reported earlier in this paper) or through use of simplified formulae. The three approaches reported by ACI (1999), Schuster (1972) and Zsutty (1968) were used in the current study and a regression analysis was conducted between non-dimensional quantities, for cases corresponding to the rib spacing of 152 mm - 305 mm. Since the number of cases for comparison is limited a reduction of 15% in the regression line was used as recommended by Porter and Ekberg (1976) with a confidence level of 95%. Resulting design equations and R² values (which indicate how well the model fits the data, e.g., a value close to 1.0 indicates that almost all the variability has been accounted for) for the 3 cases using the two extreme rib spacings are listed in Table 3 and a comparison with experimental results is shown in Table 4.

The deflection limit state can then be checked following conventional elastic theory applies to reinforced concrete members (McGregor 1997) through the use of transformed sections for the FRP components, and considered the cracked and uncracked cases. It is noted that the moment of inertia of cracked section can be determined as

$$I_c = \frac{b}{3}(h - y_u)^3 + n_4 b t_4 \left[\left(y_u - \frac{t_4}{2} \right)^2 + \frac{t_4^2}{12} \right] + n_f a_o d_s \left[2 \left(y_u - \frac{d_s}{2} \right)^2 + \frac{d_s^2}{6} \right] + n_s \left\{ (w - a_o) t_s \left[2 \left(y_u - \frac{t_4}{2} \right)^2 + \frac{t_s^2}{6} \right] + t_s d_s \left[4 \left(y_u - \frac{d_s}{2} \right)^2 + \frac{d_s^2}{3} \right] + a_o t_s \left[2 (y_u - d_s)^2 + \frac{t_s^2}{6} \right] \right\} \quad (15)$$

where the n terms are the modulus ratios, $n_4 = E_4/E_c$, $n_f = E_f/E_c$, $n_s = E_s/E_c$, for the bottom CFRP panel, the foam filler, and the web of the stiffeners, respectively. The elastic neutral axis of the moment of inertia of uncracked section, is given by

$$y_u = \frac{\sum E A y}{\sum E A} = \frac{\sum n A y}{\sum n A} = \frac{\frac{b h^2}{2} - a_o d_s^2 + n_4 b \frac{t_4^2}{2} + n_f a_o d_s^2 + n_s t_s [(w - a_o) t_4 + 2 d_s (d_s + a_o)]}{b h - 2 a_o d_s + n_4 b t_4 + 2 n_f a_o d_s + 2 n_s t_s (w + 2 d_s)} \quad (16)$$

and the moment of inertia of the uncracked section can be determined as

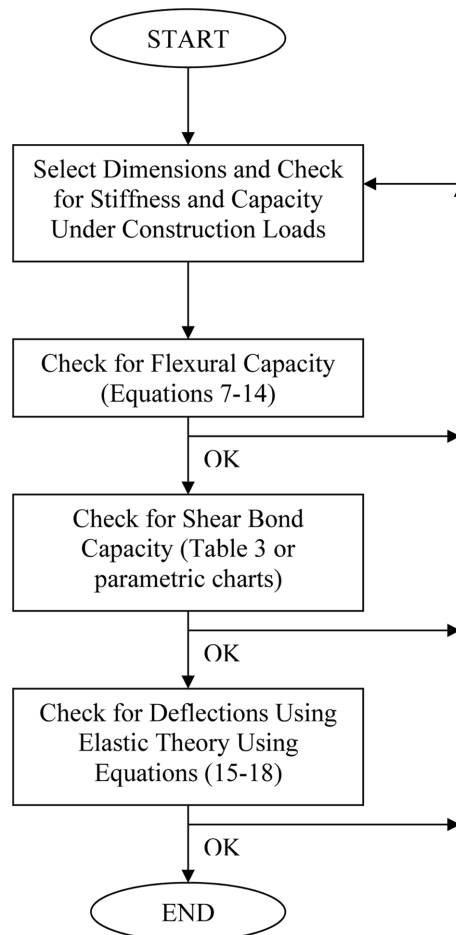


Fig. 16 Summary of design procedure for deck section

$$\begin{aligned}
 I_u = & b(h - d_s) \left[\frac{(h - d_s)^2}{12} + \left(y_u - \frac{h + d_s}{2} \right)^2 \right] + n_4 b t_4 \left[\left(y_u - \frac{t_4}{2} \right)^2 + \frac{t_4^2}{12} \right] + n_f a_o d_s \left[2 \left(y_u - \frac{d_s}{2} \right)^2 + \frac{d_s^2}{6} \right] \\
 & + n_s \left\{ (w - a_o) t_s \left[2 \left(y_u - \frac{t_4}{2} \right)^2 + \frac{t_s^2}{6} \right] + t_s d_s \left[4 \left(y_u - \frac{d_s}{2} \right)^2 + \frac{d_s^2}{3} \right] + a_o t_s \left[2 \left(y_u - \frac{d_s}{2} \right)^2 + \frac{t_s^2}{6} \right] \right\} \quad (17)
 \end{aligned}$$

For generality the effective moment of inertia of the section used in deflection calculation, I_d , can be taken as the average of the cracked, I_c , and uncracked section, I_u , moments of inertia such that

$$I_d = \frac{I_c + I_u}{2} \quad (18)$$

It is noted that this is rather simplistic but is used just as an example of the procedure. Several approaches for modified I values are available in the literature that more rigorously match the actual effective moment of the section and the approach presented in this paper is amenable to the use of these without loss in generality. The design procedure is summarized in Fig. 16.

4. Simplified design approach for the bridge system

The overall procedure for design is shown schematically in Fig. 17, with details for each step, once an approximate configuration is selected, discussed in the following.

4.1 Web shear

The maximum shear stress in the web, τ_{\max} , can be approximately taken to be equal to 1.5 times the average shear stress in the girder web (MacGregor 1997), such that

$$\tau_{\max} = 1.5(V_u/2t_w d) \quad (19)$$

such that the section's ultimate shear strength is given by

$$V_u = (4/3)t_w d \tau_{fw}^* \quad (20)$$

where τ_{fw}^* is the in-plane fracture shear strength of the web.

4.2 Web shear buckling

Following Deskovic *et al.* (1995) and experimental investigations on girder sections (Cheng *et al.* 2005) expressions determining the average web shear buckling stress, τ_{bw}^* , (Timoshenko and Gere 1961, Holmes and Just 1983) are adopted herein to provide an estimate

$$\tau_{bw}^* = \frac{4K^4 \sqrt{D_L D_T^3}}{t_w d^2} \quad \text{for } \theta > 1 \quad (21a)$$

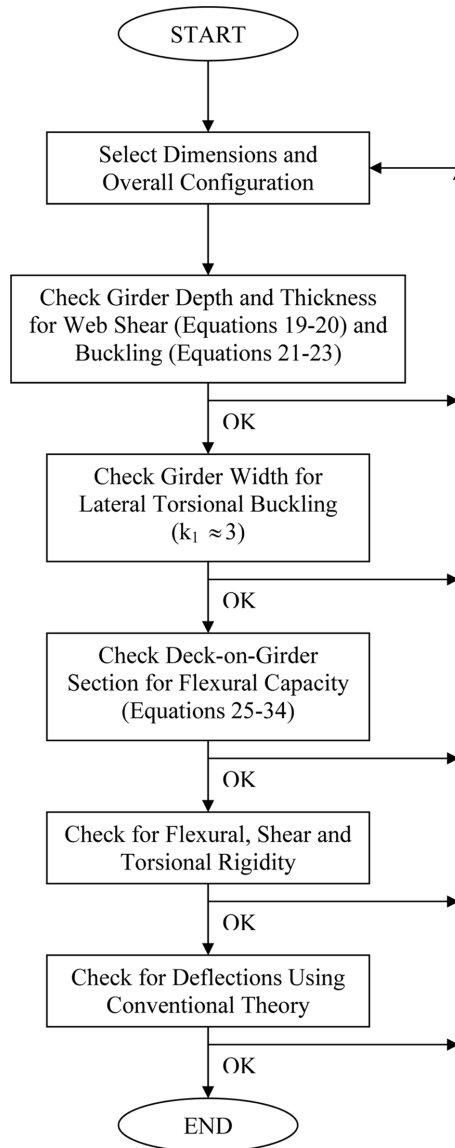


Fig. 17 Flow of steps in overall design of the slab-on-girder system

$$\tau_{bw}^* = \frac{4K^4 \sqrt{D_T H}}{t_w d^2} \quad \text{for } \theta < 1 \quad (21b)$$

where the parameter K depends on θ as listed in Table 5 (Timoshenko and Gere 1961) and D_L , D_T , H are defined as

$$\theta = \sqrt{D_L D_T} / H \quad (22a)$$

Table 5 Variation of K (Eq. (20)) with θ (Eq. (21)) following Timoshenko and Gere (1961)

θ	K
0	18.6
0.2	18.9
0.5	19.9
1.0	22.2
2.0	18.8
3.0	17.6
5.0	16.6
10.0	15.9
20.0	15.5
40.0	15.3

$$D_L = \frac{E_w t_w^3}{12(1 - \nu_L \nu_T)}, \quad D_T = \frac{E_w \tau t_w^3}{12(1 - \nu_L \nu_T)} \quad (22b)$$

$$H = \frac{1}{2}(\nu_L D_T + \nu_T D_L) + \frac{G_w t_w^3}{6(1 - \nu_L \nu_T)} \quad (22c)$$

wherein E_w is the longitudinal modulus of girder webs and E_{wT} is the transverse modulus of the webs. Then the average shear buckling force can be determined as

$$V_u = 2t_w d \tau_{b,w}^* \quad (23)$$

4.3 Lateral torsional buckling

Hollow box sections, in general, known to have a high resistance to lateral instability, which is typically assured by specifying the limit for a section's height-to-width ratio in a constraint inequality of the form

$$(d + a)/w < k_1 \quad (24)$$

where a is the depth of the anchorage zone and k_1 is the constant chosen by the designer. Deskovic *et al.* (1995) recommend that a reasonably conservative value of about 3 be used.

4.4 Flexural strength

The flexural strength of a typical slab-on-girder section is estimated following a similar methodology as explained for the FRP-concrete deck, using equilibrium principles. It should be noted that as in the deck, the neutral axis can be located in three distinct regions, for which explicit design expressions are listed in Eqs. (25)-(34).

If the neutral axis is located within the concrete slab, i.e., $d \leq y_u \leq d + D$ (as in Fig. 18(a)),

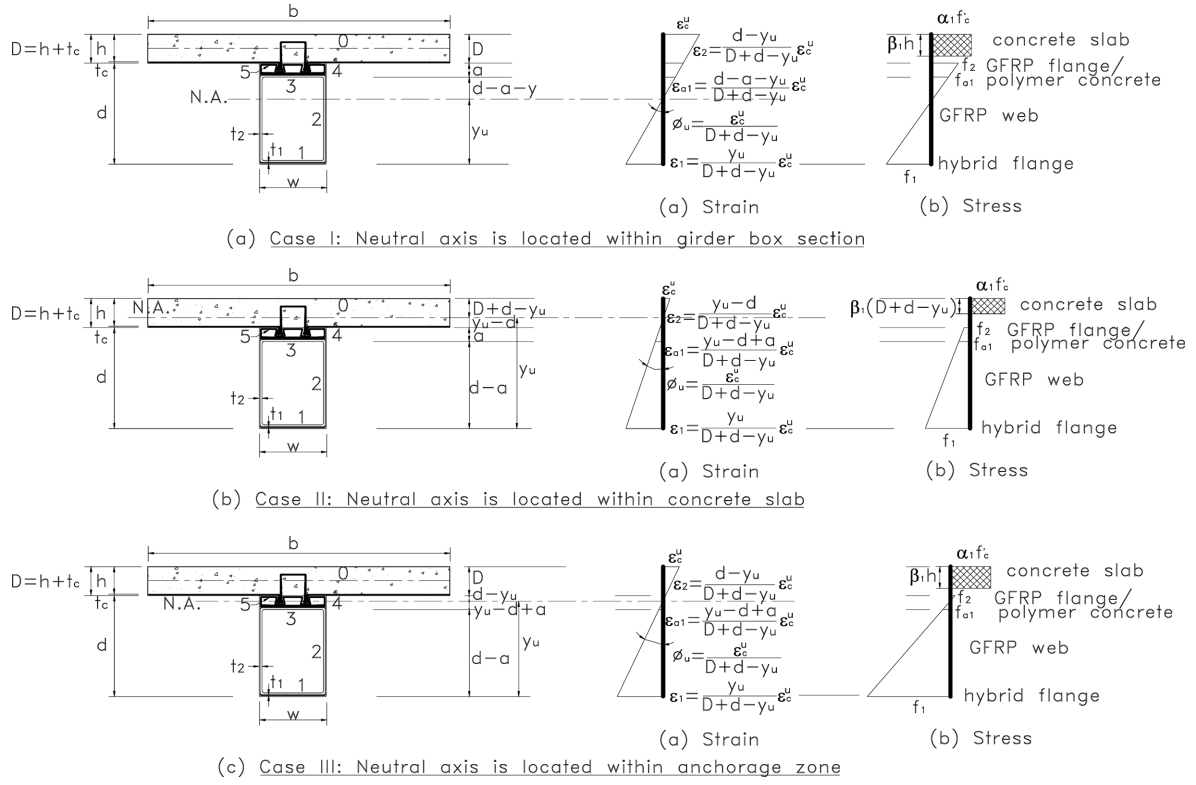


Fig. 18 Stress and strain distribution at ultimate for the slab-on-girder system

$$\varepsilon_c = \varepsilon_c^u, \quad \varepsilon_1 < \varepsilon_1^u \quad (25)$$

$$\varepsilon_1 = \frac{y_u}{D+d-y_u} \varepsilon_c^u, \quad \varepsilon_2 = \frac{y_u-d}{D+d-y_u} \varepsilon_c^u \quad (26)$$

$$\varepsilon_{a1} = \frac{y_u-d+a}{D+d-y_u} \varepsilon_c^u$$

$$y_u = D+d + C_1 / (2C_3) - [4(DC_1 + dC_1 + C_2) / C_3 + C_1^2 / C_3^2]^{1/2} / 2 \quad (27)$$

$$M_u = 0.85f_c' \beta_1 b (D+d-y_u) [(1-\beta_1/2)(D+d) + y_u \beta_1 / 2] - \frac{\varepsilon_c^u}{D+d-y_u} \left\{ [E_7(b-s)t_c d + C_4 + E_p a w (d-a/2) + E_1 t_1^2 w / 2] y_u \right\} + C_5 - E_7(b-s)t_c d^2 + E_p a w (ad - a^2/3 - d^2) \left. \right\}$$

where

$$C_1 = E_7 t_c (b-s) + E_5 t_5 (w+4a) + 2E_4 t_4 a + E_3 t_3 w + 2E_2 t_2 (d-a) + (E_p a + E_1 t_1) w \quad (28a)$$

$$C_2 = [E_4t_4a + E_5t_5(2a + l_b) + E_3t_3w + E_2t_2(d - a) + E_paw/2]a - [E_7(b - s)t_c + E_5t_5(w + 4a) + 2E_4t_4a + E_2t_2(d - a) + (E_3t_3 + E_pa)w]d \quad (28b)$$

$$C_3 = 0.85f'_c\beta_1b/\varepsilon_c^u \quad (28c)$$

$$C_4 = E_5t_5[wd - l_ba + 2a(2d - a)] + E_4t_4a(2d - a) + E_3t_3w(d - a) + E_2t_2(d - a)^2 \quad (28d)$$

If the neutral axis is located within the girder bottom section, i.e., $0 \leq y_u \leq d - a$ (as seen in Fig. 18(b)),

$$\varepsilon_1 = \frac{y_u}{D + d - y_u} \varepsilon_c^u, \quad \varepsilon_2 = \frac{d - y_u}{D + d - y_u} \varepsilon_c^u \quad (29)$$

$$\varepsilon_{a1} = \frac{d - a - y_u}{D + d - y_u} \varepsilon_c^u$$

$$y_u = [C_2 + C_3(D + d)]/(E_1t_1w + C_1 + C_3) \quad (30)$$

$$M_u = 0.85f'_c\beta_1bh(D + d - h\beta_1/2) + \varepsilon_c^u/(D + d - y_u) \{ [E_7(b - s)t_cd(d - y_u) + E_2t_2(d - a - y_u)^2(2d - 2a - y_u)/3 - E_2t_2y_u^3/3 - (C_4 + E_1t_1^2w/2)y_u] + E_paw[d(d - a/3)/2 + (d/2 - a/3)(d - a) - (d - a/2)y_u] + C_5 \}$$

where

$$C_1 = E_7t_c(b - s) + E_5t_5(w + 4a) + 2E_4t_4a + E_3t_3w + 2E_2t_2(d - a) + E_paw \quad (31a)$$

$$C_2 = [E_7t_c(b - s) + E_5t_5(l_b + 2a) + E_4t_4a]d + E_paw(d - a/2) + [E_4t_4a + E_5t_5(l_b + 2a) + E_3t_3w + E_2t_2(d - a)](d - a) \quad (31b)$$

$$C_3 = 0.85f'_c\beta_1bh/\varepsilon_c^u \quad (31c)$$

$$C_4 = E_5t_5(wd - l_ba) + (E_4t_4 + 2E_5t_5)a(2d - a) + E_3t_3w(d - a) \quad (31d)$$

$$C_5 = [E_5t_5l_b d + (E_4t_4 + 2E_5t_5)a(d - a/3)]d + [2(E_4t_4 + 2E_5t_5)a(d/2 - a/3) + E_5t_5l_b(d - a) + E_3t_3w(d - a)](d - a) \quad (31e)$$

If the neutral axis is located within the girder top anchorage zone, i.e., $d - a \leq y_u \leq d$ (Fig. 18(c)),

$$\varepsilon_1 = \frac{y_u}{D + d - y_u} \varepsilon_c^u, \quad \varepsilon_2 = \frac{d - y_u}{D + d - y_u} \varepsilon_c^u \quad (32)$$

$$\varepsilon_{a1} = \frac{y_u - d + a}{D + d - y_u} \varepsilon_c^u$$

$$y_u = [C_1 + C_3(D + d)] / (C_2 + C_3) \quad (33)$$

$$\begin{aligned} M_u = & 0.85f'_c \beta_1 bh(D + d - h\beta_1/2) + \varepsilon_c^u / (D + d - y_u) \{ [E_7(b - s)t_c d \\ & + E_5 t_5 l_t d + (E_4 t_4 + 2E_5 t_5 + E_p w/2)(d - y_u)(2d + y_u)/3](d - y_u) \\ & - [(E_4 t_4 + 2E_5 t_5)(y_u - d + a)(y_u + 2d - 2a)/3 + C_4](y_u - d + a) \\ & - [E_2 t_2 (d - a)^2/3 + E_1 t_1^2 w/2]y_u - E_p w(y_u - d + a)^2(4y_u - d + a)/6 \} \end{aligned}$$

where

$$\begin{aligned} C_1 = & [E_7 t_c (b - s) + E_5 t_5 l_t]d + (E_4 t_4 + 2E_5 t_5 + E_p w/2)a(2d - a) \\ & + [E_5 t_5 l_b + E_3 t_3 w + E_2 t_2 (d - a)](d - a) \end{aligned} \quad (34a)$$

$$C_2 = 2[E_4 t_4 + 2E_5 t_5 + E_p w/2]a + E_7 t_c (b - s) + (E_5 t_5 + E_3 t_3 + E_1 t_1)w + 2E_2 t_2 (d - a) \quad (34b)$$

$$C_3 = 0.85f'_c \beta_1 bh / \varepsilon_c^u \quad (34c)$$

$$C_4 = (E_5 t_5 l_b + E_3 t_3 w)(d - a) + 2E_2 t_2 (d - a)^2/3 \quad (34d)$$

The flexural rigidity (EI) of the slab-on-girder section (as denoted in Fig. 18) can be expressed as

$$\begin{aligned} (EI) = & [E_0 bh^3 + E_1 wt_1^3 + 2E_2 t_2 (d - a)^3 + E_3 wt_3^3 + 2E_4 t_4 a^3 + 4E_5 (t_5 a^3 + wt_5^3) + E_p wa^3 + E_7 (b - s)t_c^3]/12 \\ & + E_0 bh(d + D/2 - y)^2 + E_1 wt_1(t_1/2 - y)^2 + E_2 t_2 (d - a)(d - a - 2y)^2/2 + E_3 wt_3 (d - a - y)^2 \\ & + (2E_4 t_4 + 4E_5 t_5 + E_p w)a(d - a/2 - y)^2 + [E_5 t_5 l_t + E_7 (b - s)t_c](d - y)^2 + E_5 t_5 l_b (d - a - y)^2 \end{aligned} \quad (35)$$

where y is the depth of the centroidal axis from the girder bottom fiber and is given by

$$\begin{aligned} y = & [E_0 bh(d + D/2) + E_1 wt_1^2/2 + E_2 t_2 (d - a)^2 + E_3 wt_3 (d - a) + (2E_4 t_4 + 4E_5 t_5 + E_p w)a(d - a/2) \\ & + E_5 t_5 (wd - l_b a) + E_7 (b - s)t_c d] / [E_0 bh + E_1 wt_1 + 2E_2 t_2 (d - a) + (E_3 t_3 + E_5 t_5)w \\ & + (2E_4 t_4 + 4E_5 t_5 + E_p w)a + E_7 (b - s)t_c] \end{aligned} \quad (36)$$

The shear rigidity, GA , of the section can be determined by assuming that the shear forces are resisted by the webs of the girder only, giving a,

$$(GA) = 2G_2 t_2 (d - a) \quad (37)$$

The axial rigidity of the section can also be determined as:

$$(EA) = E_0 bh + E_1 wt_1 + 2E_2 t_2 (d - a) + (E_3 t_3 + E_5 t_5)w + (2E_4 t_4 + 4E_5 t_5 + E_p w)a + E_7 (b - s)t_c \quad (38)$$

It is noted that two basic assumptions are made in calculating the torsional rigidity of the section: (a) the equivalent shear modulus based on the transformed section method is used; and (b) the

contribution of the carbon FRP deck panel is neglected due to its negligible thickness compared to its width. Thus the torsional rigidity consists of the contribution of the box section of girder bottom with a depth of $(d - a)$, the solid rectangular section at cap region with a depth of a , and the narrow rectangular concrete slab section. Therefore the torsional rigidity can be obtained as

$$(GJ) = \frac{4[(G_1t_1 + G_3t_3)w + 2G_2(d - a)t_2](d - a)^2w^2}{[(t_1 + t_3)w + 2(d - a)t_2][2(d - a)t_2 + w/t_1 + w/t_3]} + \frac{[(2G_4t_4 + 4G_5t_5 + w)a + G_5l_1t_5]wa^3}{3[(2t_4 + 4t_5 + w)a + l_1t_5]} + \frac{G_cbt_c^3}{3} \quad (39)$$

The deflection of the section under load can then be computed using conventional means. As shown in Fig. 17, if the deflection criterion is not met the design iterations can be terminated, else the procedure is repeated with a change in on or more of the geometric or performance variables.

5. Conclusions

The paper provides elucidation of the effort of critical parameters related to the configurational details of a novel FRP structural formwork based steel-free modular bridge details at both the component and systems levels. Major effects are highlighted through a parametric study and some empirical rules for preliminary design are highlighted. In addition, details pertaining to a design methodology for the deck and the slab-on-girders system are provided using simple tools based on elastic analysis in a form amenable to ease of use. The approach accounts for the variation in position of the neutral axis of both the deck and the slab-on-girder section through a series of equations for each case enabling rapid dimensioning, followed by the checking of critical structural conditions and limit states. This provides an iterative, yet simple approach to design of bridges belonging to this new class of systems.

References

- AASHTO LRFD Bridge Design Specifications (2004), 3rd Edition, American Association of State Highway and Transportation Officials, Washington, D.C.
- ABAQUS/Standard User's Manual (2003), Version 6.4, ABAQUS Inc.
- ACI 318-95 (1995), Building Code Requirements for Reinforced Concrete (ACI 318-95) and Commentary (ACI 318R-95), American Concrete Institute, Detroit.
- Cheng, L., Zhao, L., Karbhari, V.M., Hegemier, G.A. and Seible, F. (2005), "Assessment of a steel-free fiber reinforced polymer-composite modular bridge system", *J. Struct. Eng.*, ASCE, **131**(3), 498-506.
- Cheng, L. and Karbhari, V.M. (2006), "Fatigue behavior of a steel-free FRP-concrete modular bridge deck system", *ASCE J. Bridge Eng.*, **11**(4), 474-488.
- Cheng, L. (2005), "Development of a steel-free FRP-concrete slab-on-girder modular bridge system", Dissertation submitted to the Department of Structural Engineering in partial fulfillment of the Requirements for the Degree of Doctor of Philosophy, University of California, San Diego, La Jolla, CA 92093.
- Dieter, D.A., Dietsche, J.S., Bank, L.C., Oliva, M.G and Russell, J.S. (2002), "Concrete bridge decks constructed with fiber-reinforced stay-in-place forms and grid reinforcing", *Transportation Research Record*, **1814**, 219-226.
- Deskovic, N., Triantafillou, T.C. and Meier, U. (1995), "Innovative design of FRP combined with concrete:

- Short-term behavior”, *J. Struct. Eng.*, ASCE, **121**(7), 1069-1078.
- GangaRao, H.V.S., Thippeswamy, H.K., Shekar, V. and Craigo, C. (1999), “Development of glass fiber reinforced polymer composite bridge deck”, *SAMPE J.*, **35**(4), 12-24.
- Head, P.R. (1992), “Design methods and bridge forms for the cost effective use of advanced composites in bridges”, *Proc. of the 1st Int. Conf. on Advanced Composite Materials in Bridges and Structures*, Canadian Society for Civil Engineering, Montreal, Canada, 15-30.
- Holmes, M. and Just, D.J. (1983), *GRP in Structural Engineering*, Science Publishers Ltd., London, England.
- Karbhari, V.M., Seible, F., Burgueno, R., Davol, A., Wernli, M. and Zhao, L. (2000), “Structural characterization of fiber-reinforced composite short-and medium-span bridge systems”, *Appl. Comp. Mater.*, **7**(2/3), 151-182.
- Kwon, S.C., Dutta, P.K., Kim, Y.H., Eum, S.H., Shin, D.H. and Lopez-Anido, R. (2004), “Fatigue studies of FRP composite decks at extreme environmental conditions”, *Key Engineering Materials, Advances in Fracture and Failure Prevention*, **261-263**(2), 1301-1306.
- McCormac, J.C. and Nelson, J.K., Jr. (1999), *Structural Analysis: A Classical and Matrix Approach*, John Wiley & Sons, Inc., NY.
- MacGregor, J.G. (1997), *Reinforced Concrete: Mechanics and Design*, 3rd edition, Prentice-Hall Inc., New Jersey.
- Porter, M.L. and Ekberg, C.E., Jr. (1976), “Design recommendations for steel deck floor slabs”, *J. Struct. Div.*, ASCE, **102**(11), 2121-2136.
- Schuster, R.M. (1972), “Composite steel-deck-reinforced concrete systems failing in shear-bond”, *Preliminary Report, The Ninth Congress of the International Association for Bridge and Structural Engineering*, Zurich, Switzerland, 185-191.
- Taly, N. (1998), *Design of Modern Highway Bridges*, McGraw Hill, Inc.
- Timoshenko, S.P. and Goodier J.N. (1960), *Theory of Elasticity*, Chapter 10, International Student Edition, McGraw-Hill.
- Yoshizawa, H., Wu, Z.S., Yuan, H. and Kanakubo, T. (2000), “Study on FRP-concrete interface bond performance”, *J. Materials, Concrete Structures and Pavements*, JSCE, **49**(662), 105-119.
- Zsutty, T.C. (1968), “Beam shear strength prediction by analysis of existing data”, *Proc., J. the American Concrete Institute*, November, **65**(11), 943-951.